Scripta Materialia 226 (2023) 115234

Contents lists available at ScienceDirect

Scripta Materialia

journal homepage: www.journals.elsevier.com/scripta-materialia

A remarkable toughening high-entropy-alloy wire with a bionic bamboo fiber heterogeneous structure

Shichao Zhou [a], Chunduo Dai [b], Huaxing Hou [b], Yiping Lu [c], Peter K. Liaw [d], Yong Zhang [a,e,*]

[a] *Beijing Advanced Innovation Center of Materials Genome Engineering, State Key Laboratory for Advanced Metals and Materials, University of Science and Technology Beijing, Beijing 100083, China*
[b] *Ansteel Beijing Research Institute, Beijing 102211, China*
[c] *Key Laboratory of Solidification Control and Digital Preparation Technology (Liaoning Province), School of Materials Science and Engineering, Dalian University of Technology, Dalian 116024, China*
[d] *Department of Materials Science and Engineering, The University of Tennessee, Knoxville, Tennessee 37996, United States of America*
[e] *Qinghai Provincial Key Laboratory of New Light Alloys, Qinghai University, Xining 810016, China*

ARTICLE INFO

Keywords:
Bionics
Fiber
Heterogeneous
High-entropy alloy
Wire

The bionics structure inspires a new design approach for the strength-toughness trade-off of metallic materials. In this study, a bionic bamboo fiber heterogeneous microstructure was successfully constructed in an ultrafine-grained eutectic high-entropy alloy, $AlCoCrFeNi_{2.1}$, by multi-pass cold-drawing and subsequent annealing. Such a bionic microstructure possesses a hard-B2 fiber along the axial direction embedded in the soft-face-centered-cubic (FCC)-matrix, achieving an excellent synergy of strength and ductility. Originating from this structural heterogeneity, deformation incompatibility and strain gradient generated between the B2 fiber and FCC matrix phases, causing the formation of the significant hetero-deformation-induced hardening. This hardening effect not just reinforced the FCC matrix and contributed to the excellent yield strength, also enhanced high strain-hardening and postponed the strain-localization of the brittle-B2 fiber, and furthermore increased the tensile ductility.

Pursuing materials with high strength and good ductility has always been a challenge for engineering applications and energy conservation [1–10]. Unfortunately, high-performance wires, applied in rescue equipment, suspension bridge, cable-stayed bridge, and other critical infrastructure, sometimes suffer from a serious limitation - lack of uniform tensile ductility [11,12]. For instance, the elongation of high-strength pearlitic wires reported is even as low as ~ 2%, i.e., the strength-ductility trade-off [13,14].

High-entropy alloys (HEAs) have opened up a new epoch that the alloy-design concept is drawn innovatively to the center of the phase diagram from the conventional corners [5,6,15], which provides a promising pathway to overcome the strength-ductility trade-off. Especially the eutectic HEAs (EHEAs), they possess a natural duplex phase lamellar structure, which is usually viewed as in situ composites, achieving an excellent combination of strength and ductility owing to the scarce casting flaws and the synergetic effect from the composite structure [2,16-18]. For instance, Lu et al. first developed the $AlCoCrFeNi_{2.1}$ EHEA with fine layer microstructures, possessing excellent mechanical properties at room and elevated temperatures [16]. Moreover, Shi et al. architected an ultrafine-grained $AlCoCrFeNi_{2.1}$ EHEA with lamellar phases structure further enhanced its performances by rolling and annealing [2]. As the introduction above, it is an effective pathway for improving the performances of the $AlCoCrFeNi_{2.1}$ EHEA by architecture engineering.

The bionics structure, a unique approach to engineer properties by tailoring microstructures, offers a novel avenue to achieve high-performance materials [19]. For instance, a bamboo exhibits good mechanical properties in plants owing to that its fiber structure formed along the axial direction effectively strengthens the lignin [20]. Inspired by this trend, introducing such a fiber architecture into the $AlCoCrFeNi_{2.1}$ EHEA may be a promising method to enhance its mechanical properties. Moreover, the fiber microstructure may be easily constructed from a lamellae morphology by the drawing process owing to the decrease in the radial size. Thus, in the present work, the $AlCoCrFeNi_{2.1}$ EHEA was applied to architect mechanical performances by introducing a bionic bamboo fiber heterogeneous structure with the drawing process and annealing. The detailed microstructures, mechanical responses, and corresponding mechanisms of deformation were characterized.

---

* Corresponding author.
E-mail address: drzhangy@ustb.edu.cn (Y. Zhang).

https://doi.org/10.1016/j.scriptamat.2022.115234
Received 21 September 2022; Received in revised form 18 November 2022; Accepted 7 December 2022

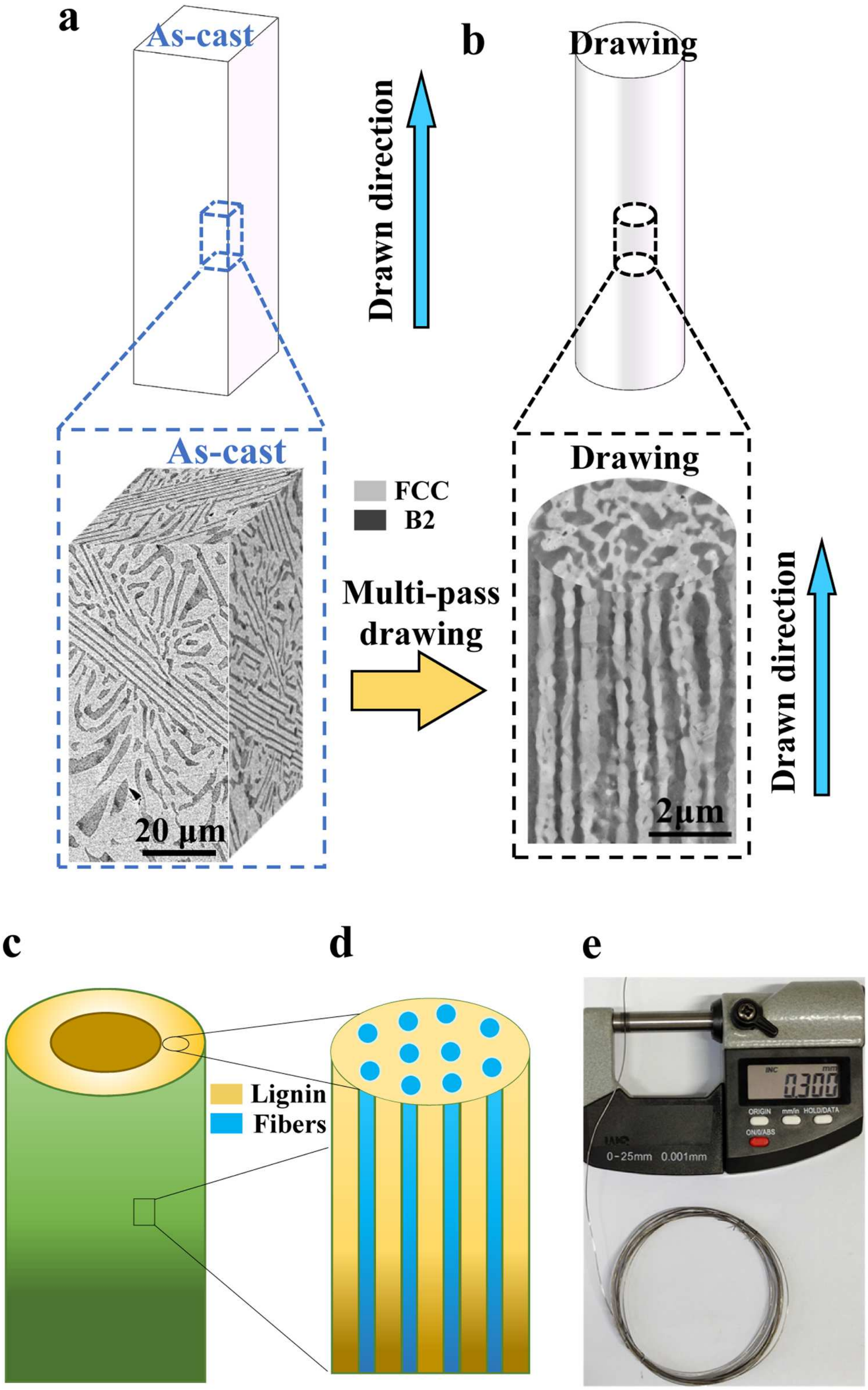

Fig. 1. Macrostructures of the $AlCoCrFeNi_{2.1}$ EHEAs. (a, b) backscattered electron (BSE) images of initial state and drawn extracted from the as-cast samples and drawn BFH wires. The blue arrow indicates the drawing direction, which is also parallel the growing direction of the fiber and the tensile loading direction. (c, d) Schematics of the bamboo and its interior fiber microstructure. (e) The photography of the $AlCoCrFeNi_{2.1}$ BFH wire with the diameter of ~ 0.3 mm.

Alloy ingots with a nominal composition of $AlCoCrFeNi_{2.1}$ (atomic percent, at.%) with approximately 2.5 kg were melted at least five times before drop-casting into a Φ55 × 220 mm MgO crucible. The alloy-process details were elaborated in previous studies [16]. Samples with 1 × 1 × 150 mm were extracted from the as-cast ingots by electrical discharge machining and then subjected to multi-pass cold-drawing at ambient temperatures to a ~ 90% reduction in the cross-sectional area. A minor deformation degree upon each drawing step (~ 0.02 mm reduction in diameter) and a moderate drawing velocity (~ 200 mm / min) were conducted. Thus, the annealing treat after each drawing step is not required. The final diameter of the cold-drawing wire is ~ 0.3 mm. After all drawing steps above, $AlCoCrFeNi_{2.1}$ wires were further

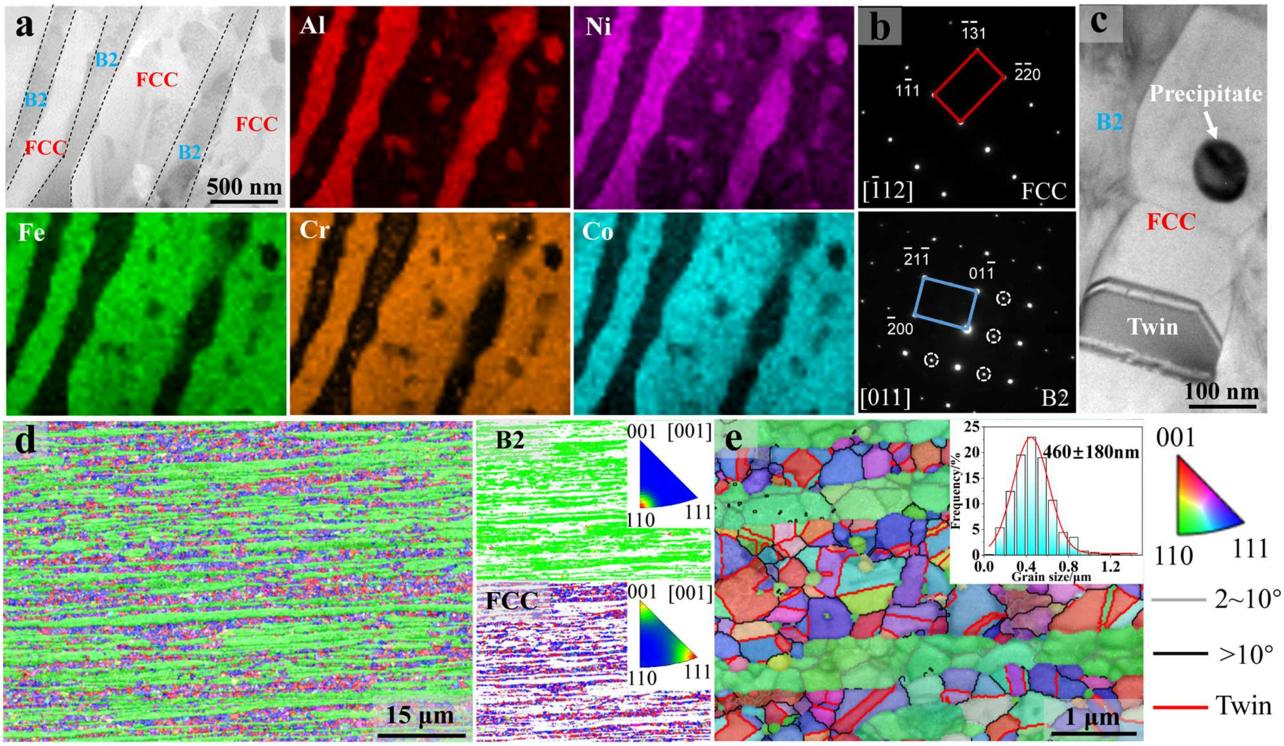

Fig. 2. Microstructures of the AlCoCrFe$Ni_{2.1}$ BFH wire. (a) STEM image showing the alternative dark-B2 fiber as well as tint-FCC matrix phases (interfaces between the FCC matrix and B2 fiber are indicated by dash lines) and EDS maps of the elemental distribution of Al, Ni, Fe, Cr, and Co. (b) SADPs of FCC and B2 phases. White circles show superlattice-diffraction spots in the B2 phase. (c) The bright-field image displaying the precipitate and annealing twin in the FCC matrix. (d) Left: EBSD images showing the whole IPF map of the BFH wire. Right: IPF maps of the B2 phase and FCC phase, respectively. (e) Enlarged IPF map showing the grain morphology and annealing-twin boundaries (pink lines). (For interpretation of the references to colour in this figure legend, the reader is referred to the web version of this article.)

annealed at various temperatures (650 °C, 700 °C, and 750 °C for 1 h in air, respectively, correspondingly denoted as BFH 650, BFH 700, and BFH 750), followed by air cooling. Microstructure characterizations were performed by a Zeiss Supra 55 field emission scanning electron microscope (SEM) equipped with an electron back-scattering diffraction (EBSD) system and a Tecnai G2 F30 S-TWIN transmission electron microscope (TEM) operated at 300 kV. For the SEM and EBSD observations, specimens were mechanically ground by a 2500-grit SiC paper and then electro-chemically polished in a mixture of 90% ethanol and 10% perchloric acid (volume percent, vol.%) with a direct voltage of 20 V at ambient temperature. The EBSD analysis was carried out using a step size of 0.02 μm at the acceleration voltage of 20 KV. The TEM samples were mechanically grinded to ~ 30 μm thickness and subsequently thinned by a Model 691.CS ion beam thinner. The quasi-static uniaxial tensile tests were performed by a Material Testing System (MTS) system with a constant strain rate of 1×10^{-3} s^{-1} at room temperature. To confirm tensile-property reproducibility, at least 3 tensile tests were conducted for each treatment condition. The tensile interruption tests were performed at the designated strain values of ~ 5%, ~ 15%, and ~ 30% (failure strain) for microstructural characterizations. The selected areas at different designated strains were extracted from the middle of the gage length or near the fracture. Tensile load-unload-reload (LUR) experiments were conducted by the same MTS machine at ambient temperature. The specimen was first stretched to a certain strain with the strain rate of 1×10^{-3} s^{-1}, and then unloaded by the load-control mode to 4 N at the unloading rate of 40 N·min^{-1}, subsequently reloaded to the next designated unloading strain. Both the quasi-static uniaxial tensile and LUR tests specimens with a gage length of ~ 70 mm were prepared carefully by electro-discharge machining.

The as-cast AlCoCrFe$Ni_{2.1}$ EHEA shows a typical lamella morphology, as presented from the three-dimensional (3D) stereographic microstructures (Fig. 1a). To date, EHEAs usually show such an alternate phase lamella morphology [2,16] or equiaxed duplex phases microstructure [17] at each 3D perspective. Nevertheless, the diversity of microstructures may enrich their mechanical properties, such as the unusual bimodal structure overcoming the trade-off of strength and ductility [4]. As shown in Fig. 1a and b, the lamellae morphology successfully evolved into a fiber-microstructure after the drawing process along the axial direction, which is easy to recognize particularly at the cross-section perspective. Similar to the brown-lignin and blue-fiber in the bamboo (Fig. 1c and d), the current fiber-structure features a tint-face-centered-cubic (FCC)-matrix phase and dark-ordered-body-centered-cubic (B2)-fiber phase. The blue arrow indicates the drawing direction, which is also parallel the growing direction of the fiber and the tensile loading direction in Fig. 3. Moreover, the diversity of the hard-B2 fiber and soft-FCC matrix successfully imparts the structural heterogeneity [21]. Thus, such a structure in Fig. 1b is hereafter referred to as the bionic bamboo fiber heterogeneous (BFH) structure, and the AlCoCrFe$Ni_{2.1}$ EHEAs wires with different annealing conditions of 650, 700, and 750°C for 1 h corresponding as BFH 650, BFH 700, and BFH 750, as described before. The photography of the drawn AlCoCrFe$Ni_{2.1}$ BFH wire with a diameter of ~ 0.3 mm is displayed in Fig. 1e.

Fig. 2a displays the scanning TEM image and corresponding energy-dispersive-spectroscopy (EDS) maps of the longitudinal section in BFH EHEAs. There are the apparent dark-B2 fiber phase and tint-FCC matrix phase, consisting with the Fig. 1b. Additionally, the EDS maps show the enriched Fe, Cr, and Co in the FCC matrix, while abundant Ni and Al in the B2 phase. The corresponding selected-area-diffraction patterns (SADPs) of FCC and B2 phases are shown in Fig. 2b. The volume fractions of FCC and B2 phases are 55.4 ± 3% and 44.6 ± 3%, respectively (Fig. 2d). Additionally, separated B2 particles embedded in the FCC

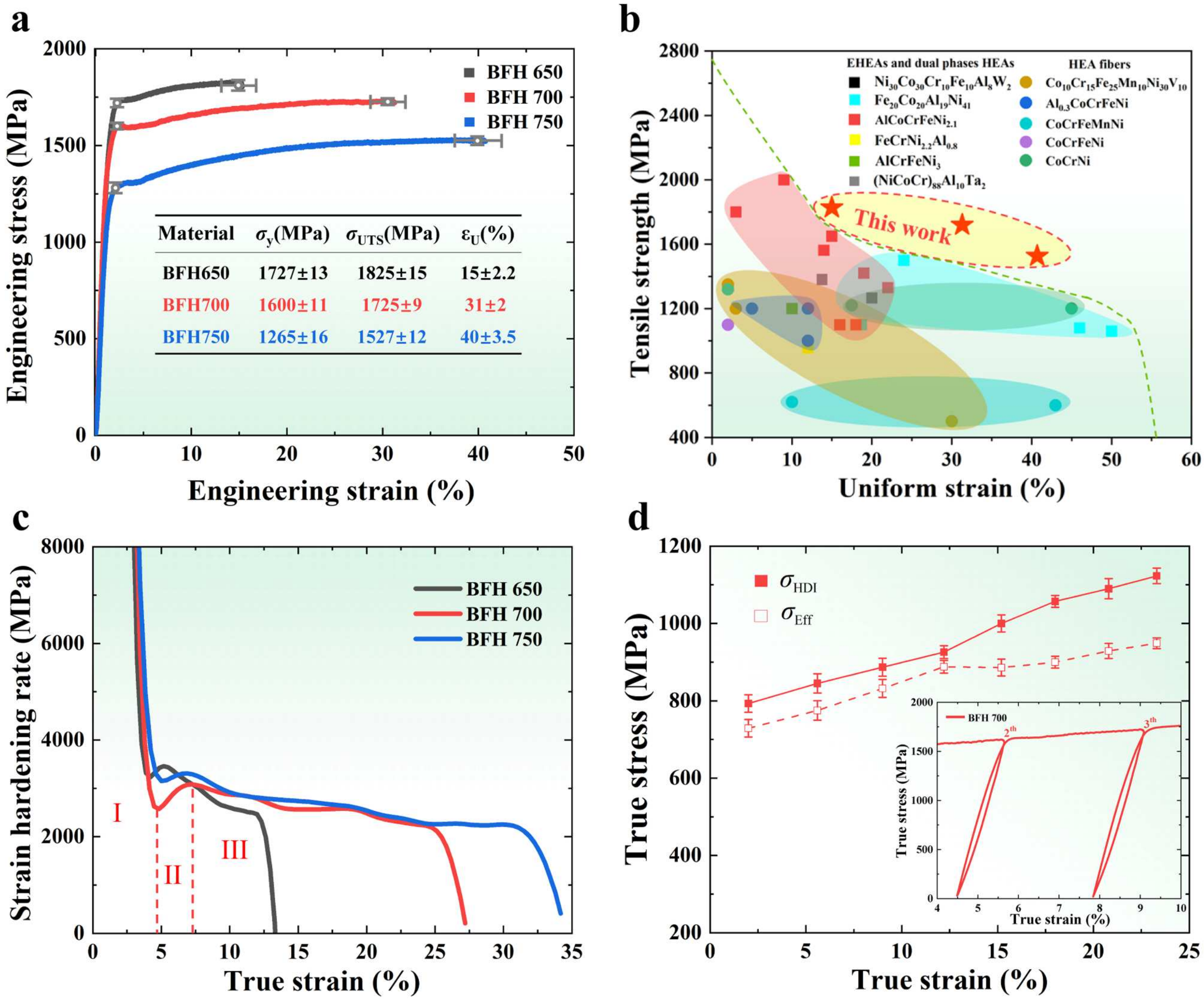

Material	σ_y(MPa)	σ_{UTS}(MPa)	ε_U(%)
BFH650	1727±13	1825±15	15±2.2
BFH700	1600±11	1725±9	31±2
BFH750	1265±16	1527±12	40±3.5

Fig. 3. Mechanical responses of the $AlCoCrFeNi_{2.1}$ BFH wires. (a) Engineering stress-strain curves of the BFH 650, 700, and 750, respectively. The inset showing detailed tensile properties. The yield strength, ultimate tensile strength, and uniform elongation are expressed here in a usual way in terms of σ_y, σ_{UTS}, and ε_U, respectively. (b) Tensile-strength and uniform-strain comparison of our $AlCoCrFeNi_{2.1}$ BFH HEA wires with previously reported EHEAs and HEA fibers. EHEAs: $Ni_{30}Co_{30}Cr_{10}Fe_{10}Al_8W_2$ [29], $Fe_{20}Co_{20}Al_{19}Ni_{41}$ [30], $AlCoCrFeNi_{2.1}$ [2], $FeCrNi_{2.2}Al_{0.8}$ [31], $AlCrFeNi_3$ [32]. HEAs fibers: $Co_{10}Cr_{15}Fe_{25}Mn_{10}Ni_{30}V_{10}$ [22], $Al_{0.3}CoCrFeNi$ [23], CoCrFeMnNi [24,27], CoCrFeNi [26], CoCrNi [11,28], $(NiCoCr)_{88}Al_{10}Ta_2$ [33]. (c) The corresponding strain-hardening curves. (d) The evolution of the HDI stress (σ_{HDI}) and effective stress (σ_{Eff}) with the variation of true strains for BFH 700. The inset shows magnified LUR cycles, which presents typical hysteresis loops for the BFH 700. The whole LUR curves and calculation details of HDI stress are shown in the supplementary Figs. S2 and S3.

matrix owing to the phase decomposition (Fig. 2a and c), which is similar to previously reported studies [2]. The B2 fiber and FCC matrix consist of recrystallized ultrafine grains, and the average diameter of both phases are roughly comparable (~ 460 nm) by the classical line intercept methods excluding the twin boundaries (Fig. 2e). Furthermore, the formation of abundant annealing twins in the FCC matrix reduced the grains size.

The whole inverse pole figure (IPF) of the $AlCoCrFeNi_{2.1}$ BFH wire is shown in Fig. 2d. For the easy observation of orientation distributions, the IPF maps of B2 and FCC phases are shown, respectively. The B2 phase indicates a $\langle 110 \rangle$ // axial direction texture while the FCC phase reveals preferred $\langle 111 \rangle$ // axial direction and minor $\langle 100 \rangle$ // axial direction texture components, all of which indicate a typical fiber texture. This distribution of fiber orientations is widely reported in previous studies [22–25].

Furthermore, we measured the mechanical behaviors of our BFH 650, BFH 700, and BFH 750 HEAs (Fig. 3). The remarkable strength-ductility synergism and corresponding strain-hardening curves of the three BFH wires are shown in Fig. 3a and c. The inset table of Fig. 3a presents the detailed tensile properties. To emphasize the excellent properties, we compared the tensile strength and uniform strain of our $AlCoCrFeNi_{2.1}$ BFH wires with previously reported EHEAs and HEA fibers [11,22-24,26-28] (Fig. 3b). Our three BFH wires locate at the upper right corner of the map, exhibiting an unusual combination of tensile strength and uniform strain. Such superior mechanical properties expand known performance boundaries, overcoming the trade-off of strength and ductility.

The high yield strength, apparent discontinuous yielding, and distinguished multi-stages strain-hardening behavior can be observed, and each strain-hardening curve comprises roughly three stages, i.e., quick drop (I), upturning to the maximum (II), and sustaining until to drop slowly (III), as partitioned by red dash lines in Fig. 3c. The present phenomenon is usually shown in heterogeneous-structures metallic materials [2,4]. The quick drop behavior of strain hardening at stage I is due to the absence of mobile dislocations, leading to that they cannot accommodate the strain rate (1×10^{-3} s^{-1}) [34]. In region II, the dislocations quickly proliferate and tangle, causing a sharp increase of strain-hardening [35]. The high strain-hardening ability in the region III

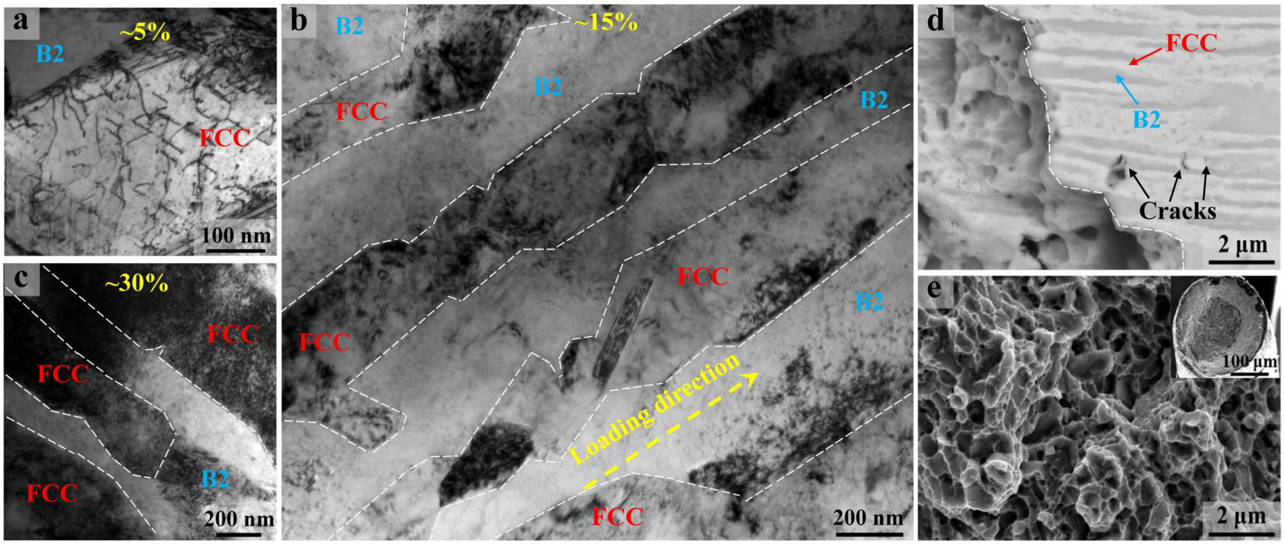

Fig. 4. Evolution of microstructures of the AlCoCrFeNi$_{2.1}$ BFH 700 wire upon tensile deformation. (a-c) TEM images of the microstructure evolution at engineering strains of ~ 5%, ~ 15%, and ~ 30%, respectively. (a) Dislocations activated in the FCC matrix appear in comparison to no apparent dislocations in the B2 fiber (at the strain of ~ 5%). (b) As the strain increased (~ 15%), the FCC matrix exhibits denser dislocations than the B2 fiber. (c) The microstructure stretched to fracture (~ 30%) shows significant pronounced dislocations in the FCC matrix and B2 fiber. (d) SEM image of the microstructure after failure near the fracture region. The longitudinal and tear sections were divided by the white dash line. (e) High-magnification fractography consisting of massive dimples (the inset presents the macroscopic fractography).

may result from the hetero-deformation-induced (HDI) effect especially for BFH 700 and 750 alloys, which show apparent sustaining hardening behavior [21].

To clarify the origin of the high yield and excellent strain-hardening ability, the tensile load-unload-reload (LUR) tests and the evolution of microstructures of the BFG 700, as a representative of BFG specimens due to the similar mechanical responses, were conducted. As displayed in the inset of Fig. 3d, local magnified LUR curves exhibited the typical hysteresis loops, implying a strong Bauschinger effect even though at the initial straining stage [35]. The whole LUR curves are presented in the supplementary (Fig. S2). The contributions of the long-range HDI stress (σ_{HDI}) and short-range effective stress (σ_{Eff}) to the macroscopic flow stress (σ_{F}) can be estimated as usual by the following equations, i.e., $\sigma_{\mathrm{HDI}} = (\sigma_{\mathrm{r}} + \sigma_{\mathrm{u}}) / 2$ and $\sigma_{\mathrm{Eff}} = (\sigma_{\mathrm{F}} - \sigma_{\mathrm{HDI}})$, where σ_{u} and σ_{r} are the unloading yield stress and the reloading yield stress, respectively. The measurement detail is referred to Yang et al. [35]. Fig. 3d shows the high initial σ_{HDI} (~ 800 MPa) and a steady increase trend with loading, which is the main origin of the high strength and strain-hardening. Thus, we will mainly discuss about the HDI- hardening effect.

The formation of the HDI stress mainly resulted from the deformation incompatibility between the hard-B2 fiber and the soft-FCC matrix [21]. Upon tensile deformation, due to the natural soft/hard distributions, the soft-FCC matrix is prone to originate plastic strains than the hard-B2 fiber. Thus, the dislocations activated firstly in the FCC matrix in comparison to no apparent dislocations in the B2 fiber (Fig. 4a) in our BFH alloys. However, such a soft-FCC matrix is unable to deform freely owing to the constraint by the hard-B2 phase. At this moment, the B2 fiber is still in the elastic deformation, causing the formation of a strain gradient between those elastic-B2 fiber and plastic-FCC matrix [2]. To accommodate this strain gradient, geometrically necessary dislocations (GNDs) formed, which induced the directional back-stress in the soft matrix and made it stronger as hard-B2 fiber [4]. Consequently, at this elastic-plastic deformation stage, the back-stress induced the HDI hardening and effectively enhanced the yield strength of our BFH EHEAs [21].

As loading increases, both the FCC matrix and B2 fiber generated plastic deformation. Owing to the soft-FCC matrix is easier to deform than the hard fiber, the former bore higher strains [21]. Thus, the deformation incompatibility still existed and further became lager with the increase of strain [4]. Much more GNDs in both the FCC matrix and B2 fiber (a corresponding forward-stress) were required to accommodate the present strain gradient, which further contributed to the increase of the HDI stress [2]. Correspondingly, the FCC matrix exhibited denser dislocations than the B2 fiber (Fig. 4b, c). The increasing HDI stress not just effectively enhanced flow stress and strain hardening, and also contributed to the initiation of more and harder slip systems, promoting dislocations nucleation and proliferation [36,37]. This theory indicated that the HDI tress contributed to the delay of the strain localization in the brittle-B2 fiber, the improvement of its strain hardening, and the increase of the effective stress. Consequently, at this co-plastic deformation stage, the synergism of the back-stress in the FCC matrix and forward-stress in the B2 fiber produced the HDI hardening [21], which contributed to the high strain hardening and good ductility.

Different from the long-range HDI stress (dislocations interactions within a large area), the short-range effective stress is related to local interactions, including the Peierls stress and forest hardening [4]. Massive GNDs increased the total dislocations density, facilitated the interactions of dislocations, and contributed to the effective stress.

Different from the previous study [2], the SEM image shows only a few microcracks near the failure and a typical fiber structure at fracture, agreeing with the BFH structure, as introduced above (Fig. 4d). Moreover, as presented at the right longitudinal section, cracks could form in both the FCC matrix and B2 fiber phases. Massive dimples are shown in the left tear section and fracture surface (Fig. 4e), indicating a ductile fracture mode and corresponding to the excellent tensile ductility (the inset shows the macroscopic fractography).

In conclusion, we have successfully introduced a bionic bamboo-fiber heterogeneous structure into AlCoCrFeNi$_{2.1}$ BFH EHEAs by the drawing process. The architected BFH wires possess an extraordinary synergism of strength and ductility, overcoming the strength-ductility trade-off. The detailed microstructure analysis and LUR tests indicated that the excellent HDI-hardening effects are mainly responsible for the unusual strength and high strain hardening. Additionally, the HDI effect postponed the strain localization of the brittle-B2 fiber, which contributed to the tensile ductility. The present work provides a guidance for developing fiber-heterogeneous structure eutectic alloys with high performance.

Declaration of Competing Interest

The authors declare that they have no known competing financial interests or personal relationships that could have appeared to influence the work reported in this paper.

Acknowledgments

Shichao Zhou Thanks Zhiran Yan and Yimin Cui for their help with discussions. This work was supported by the Guangdong Basic and Applied Basic Research Foundation [No. 2019B1515120020]; the Funds for Creative Research Groups of China [No. 51921001]; and Mechanism Research and Preparation Technology of High Entropy Alloys with Ultra-high Strength [No. 2020–0531]. P.K.L. very much appreciates the supports from (1) the National Science Foundation (DMR-1611180 and 1809640) and (2) the US Army Research Office (W911NF-13–1–0438 and W911NF-19–2–0049).

Supplementary materials

Supplementary material associated with this article can be found, in the online version, at doi:10.1016/j.scriptamat.2022.115234.

References

[1] T.W. Zhang, S.G. Ma, D. Zhao, Y.C. Wu, Y. Zhang, Z.H. Wang, J.W. Qiao, Simultaneous enhancement of strength and ductility in a NiCoCrFe high-entropy alloy upon dynamic tension: micromechanism and constitutive modeling, Int. J. Plasticity 124 (2020) 226–246.
[2] P. Shi, W. Ren, T. Zheng, Z. Ren, X. Hou, J. Peng, P. Hu, Y. Gao, Y. Zhong, P. K. Liaw, Enhanced strength–ductility synergy in ultrafine-grained eutectic high-entropy alloys by inheriting microstructural lamellae, Nat. Commun. 10 (1) (2019).
[3] Y. Zhang, T.T. Zuo, Z. Tang, M.C. Gao, K.A. Dahmen, P.K. Liaw, Z.P. Lu, Microstructures and properties of high-entropy alloys, Prog. Mater. Sci. 61 (2014) 1–93.
[4] X. Wu, M. Yang, F. Yuan, G. Wu, Y. Wei, X. Huang, Y. Zhu, Heterogeneous lamella structure unites ultrafine-grain strength with coarse-grain ductility, P. Natl. Acad. Sci. USA 112 (47) (2015) 14501–14505.
[5] X. Yan, Y. Zhang, A body-centered cubic $Zr_{50}Ti_{35}Nb_{15}$ medium-entropy alloy with unique properties, Scripta Mater. 178 (2020) 329–333.
[6] X. Yan, Y. Zhang, Functional properties and promising applications of high entropy alloys, Scripta Mater. 187 (2020) 188–193.
[7] O.N. Senkov, G.B. Wilks, D.B. Miracle, C.P. Chuang, P.K. Liaw, Refractory high-entropy alloys, Intermetallics 18 (9) (2010) 1758–1765.
[8] T. Yang, Y.L. Zhao, Y. Tong, Z.B. Jiao, J. Wei, J.X. Cai, X.D. Han, D. Chen, A. Hu, J. J. Kai, K. Lu, Y. Liu, C.T. Liu, Multicomponent intermetallic nanoparticles and superb mechanical behaviors of complex alloys, Science 362 (6417) (2018) 933–937.
[9] Z. Li, K.G. Pradeep, Y. Deng, D. Raabe, C.C. Tasan, Metastable high-entropy dual-phase alloys overcome the strength–ductility trade-off, Nature 534 (7606) (2016) 227–230.
[10] B. Gludovatz, A. Hohenwarter, D. Catoor, E.H. Chang, E.P. George, R.O. Ritchie, A fracture-resistant high-entropy alloy for cryogenic applications, Science 345 (6201) (2014) 1153–1158.
[11] J. Liu, J. Chen, T. Liu, C. Li, Y. Chen, L. Dai, Superior strength-ductility CoCrNi medium-entropy alloy wire, Scripta Mater. 181 (2020) 19–24.
[12] M. Zelin, Microstructure evolution in pearlitic steels during wire drawing, Acta Mater. 50 (17) (2002) 4431–4447.
[13] X. Zhang, N. Hansen, A. Godfrey, X. Huang, Dislocation-based plasticity and strengthening mechanisms in sub-20 nm lamellar structures in pearlitic steel wire, Acta Mater. 114 (2016) 176–183.
[14] X.D. Zhang, A. Godfrey, W. Liu, Q. Liu, Study on dislocation slips in ferrite and deformation of cementite in cold drawn pearlitic steel wires from medium to high strain, Mater. Sci. Tech-Long 27 (2) (2011) 562–567.
[15] N. Xu, S. Li, R. Li, M. Zhang, Z. Yan, Y. Cao, Z. Nie, Y. Ren, Y. Wang, In situ investigation of the deformation behaviors of $Fe_{20}Co_{30}Cr_{25}Ni_{25}$ and $Fe_{20}Co_{30}Cr_{30}Ni_{20}$ high entropy alloys by high-energy X-ray diffraction, Mat. Sci. Eng. A-Struct. 795 (2020), 139936.
[16] Y. Lu, Y. Dong, S. Guo, L. Jiang, H. Kang, T. Wang, B. Wen, Z. Wang, J. Jie, Z. Cao, H. Ruan, T. Li, A promising new class of high-temperature alloys: eutectic high-entropy alloys, Sci. Rep. 4 (2014), 6200.
[17] I.S. Wani, T. Bhattacharjee, S. Sheikh, Y. Lu, S. Chatterjee, P. Bhattacharjee, S. Guo, N. Tsuji, Ultrafine-grained $AlCoCrFeNi_{2.1}$ eutectic high-entropy alloy, Mater. Res. Lett. 4 (3) (2016).
[18] J. Miao, H. Yao, J. Wang, Y. Lu, T. Wang, T. Li, Surface modification for $AlCoCrFeNi_{2.1}$ eutectic high-entropy alloy via laser remelting technology and subsequent aging heat treatment, J. Alloy. Compd. 894 (2022), 162380.
[19] C. Wei, X. Zhang, P. Hu, W. Han, G. Tian, The fabrication and mechanical properties of bionic laminated ZrB2–SiC/BN ceramic prepared by tape casting and hot pressing, Scripta Mater. 65 (9) (2011) 791–794.
[20] C. Chen, Z. Li, R. Mi, J. Dai, H. Xie, Y. Pei, J. Li, H. Qiao, H. Tang, B. Yang, L. Hu, Rapid processing of whole bamboo with exposed, aligned nanofibrils toward a high-performance structural material, ACS Nano 14 (5) (2020) 5194–5202.
[21] Y. Zhu, X. Wu, Perspective on hetero-deformation induced (HDI) hardening and back stress Mater, Res. Lett. 7 (10) (2019) 393–398.
[22] H.S. Cho, S.J. Bae, Y.S. Na, K.S. Lee, J.H. Kim, D.G. Lee, Influence of reduction ratio on the microstructural evolution and subsequent mechanical properties of cold-drawn $Co_{10}Cr_{15}Fe_{25}Mn_{10}Ni_{30}V_{10}$ high entropy alloy wires, J. Alloy. Compd. 821 (2020), 153526.
[23] D. Li, C. Li, T. Feng, Y. Zhang, G. Sha, J.J. Lewandowski, P.K. Liaw, Y. Zhang, High-entropy $Al_{0.3}CoCrFeNi$ alloy fibers with high tensile strength and ductility at ambient and cryogenic temperatures, Acta Mater. 123 (2017) 285–294.
[24] X. Ma, J. Chen, X. Wang, Y. Xu, Y. Xue, Microstructure and mechanical properties of cold drawing CoCrFeMnNi high entropy alloy, J. Alloy. Compd. 795 (2019) 45–53.
[25] J. Chen, Yan W, J. Miao, Microstructure and texture evolution of cold-drawn <111>single-crystal copper, Metall. Mater. Trans. A 42A (2011) 2373–2383.
[26] W. Huo, F. Fang, H. Zhou, Z. Xie, J. Shang, J. Jiang, Remarkable strength of CoCrFeNi high-entropy alloy wires at cryogenic and elevated temperatures, Scripta Mater. 141 (2017) 125–128.
[27] Y.J. Kwon, J.W. Won, S.H. Park, J.H. Lee, K.R. Lim, Y.S. Na, C.S. Lee, Ultrahigh-strength CoCrFeMnNi high-entropy alloy wire rod with excellent resistance to hydrogen embrittlement, Mat. Sci. Eng. A-Struct. 732 (2018) 105–111.
[28] J. Chen, Y. Chen, J. Liu, T. Liu, L. Dai, Anomalous size effect in micron-scale CoCrNi medium-entropy alloy wire, Scripta Mater. 199 (2021), 113897.
[29] Q. Wu, Z. Wang, T. Zheng, D. Chen, Z. Yang, J. Li, J. Kai, J. Wang, A casting eutectic high entropy alloy with superior strength-ductility combination, Mater. Lett. 253 (2019) 268–271.
[30] X. Jin, Y. Zhou, L. Zhang, X. Du, B. Li, A novel $Fe_{20}Co_{20}Ni_{41}Al_{19}$ eutectic high entropy alloy with excellent tensile properties, Mater. Lett. 216 (2018) 144–146.
[31] X. Jin, J. Bi, L. Zhang, Y. Zhou, X. Du, Y. Liang, B. Li, A new $CrFeNi_2Al$ eutectic high entropy alloy system with excellent mechanical properties, J. Alloy. Compd. 770 (2019) 655–661.
[32] Y. Dong, Z. Yao, X. Huang, F. Du, C. Li, A. Chen, F. Wu, Y. Cheng, Z. Zhang, Microstructure and mechanical properties of $AlCo_xCrFeNi_{3\text{-}x}$ eutectic high-entropy-alloy system, J. Alloy. Compd. 823 (2020), 153886.
[33] D. Zhang, J. Zhang, J. Kuang, G. Liu, J. Sun, The B2 phase-driven microstructural heterogeneities and twinning enable ultrahigh cryogenic strength and large ductility in NiCoCr-based medium-entropy alloy, Acta Mater. 233 (2022), 117981.
[34] X. Huang, N. Hansen, N. Tsuji, Hardening by annealing and softening by deformation in nanostructured metals, Science 312 (5771) (2006) 249–251.
[35] M. Yang, Y. Pan, F. Yuan, Y. Zhu, X. Wu, Back stress strengthening and strain hardening in gradient structure, Mater. Res. Lett. 4 (3) (2016) 145–151.
[36] Y. Wang, M. Yang, X. Ma, M. Wang, K. Yin, A. Huang, C. Huang, Improved back stress and synergetic strain hardening in coarse-grain/nanostructure laminates, Mat. Sci. Eng. A-Struct. 727 (2018) 113–118.
[37] Y. Wang, M. Chen, F. Zhou, High tensile ductility in a nanostructured metal, Nature 419 (2002) 912–915.